Long-term variability of the Kuroshio transport east of Taiwan and the climate it conveys

Mao-Lin Shen [a], Yu-Heng Tseng [b,*], Sen Jan [c], Chih-Chieh Young [d,1], Ming-Da Chiou [c]

[a] Geophysical Institute, University of Bergen, Norway
[b] Climate and Global Dynamics Division, National Center for Atmospheric Research, USA
[c] Institute of Oceanography, National Taiwan University, Taiwan
[d] Department of Atmospheric Sciences, National Taiwan University, Taiwan

A R T I C L E   I N F O

Article history:
Available online 6 November 2013

A B S T R A C T

The Kuroshio transport (KT) was established using satellite altimetry data from 1993 to 2010 via three methods: the geostrophic relationship (GR), the empirical relationship (ER), and the transfer function (TF). The relationships were built on the observed KT from the World Ocean Circulation Experiment moored current meter array east of Taiwan (referred to as PCM-1) and its surrounding sea surface height (SSH) difference. Using a modeled 10-year climatology run of the KT, we verify the three methods and associated characteristics in long-term applications. The GR could not capture high-frequency variability of less than four months well. The KT approximated by the ER had a similar variation with a weaker magnitude and the transport was underestimated. Although the TF can establish signals from all available frequency domains, results suggest that the observational period of PCM-1 may be too short to build a reliable TF. The KT estimated by both the GR and the TR was subsequently used to analyze the long-term variability of the KT in the PCM-1 line. The annual averaged KT was influenced by the northern branch of the North Equatorial Current that was affected primarily by El Niño-Southern Oscillation events. The anomaly of the KT was dominated by mesoscale eddies east of Taiwan resulting from the influence of the West Pacific (WP) teleconnection pattern. Correlation analysis confirmed that the long-term KT in the PCM-1 line conveys not only the ENSO signal but the WP teleconnection, which connects the tropic and extratropic dynamics together.

© 2013 Elsevier Ltd. All rights reserved.

1. Introduction

Knowledge of the Kuroshio transport (KT) variability is vital to understanding the North Pacific current system and ocean–atmosphere climate feedback. The western boundary current plays a critical role in air–sea interactions (Kwon et al., 2010) and carries large amounts of heat from the tropical to the extratropical ocean (Zhang et al., 2002); see Fig. 1 for an overview of the western North Pacific current system. Spanning from the eastern Philippines to the southern Okinawa trough, the KT is approximately 20 Sv along the East Taiwan Channel (ETC) and conveys tropical Pacific water mass to the subtropical Pacific (Chen, 2005). The KT variability affects the flow pattern around Taiwan, e.g., the variation of the Taiwan Strait outflow (Centurioni et al., 2004; Hu et al., 2000, 2010; Jan et al., 2010) and the Luzon Strait Throughflow (LST) (Caruso et al., 2006; Chern et al., 2010; Matsuno et al., 2009; Yu et al.,

2007), as well as the occurrence of the cold-dome northeast of Taiwan (Shen et al., 2011). Additionally, the KT variability along the ETC has considerable downstream effects such as impacting the interaction of the continental water of the East China Sea (ECS) and Kuroshio water (Chen, 2008; Chen and Sheu, 2006; Chen et al., 1995; Lee and Takeshi, 2007; Ma et al., 2010; Tang et al., 2000). These may further affect the variability of the KT south of Japan (Akitomo et al., 1996), the meander path off the shore of the Japan coast, and the Kuroshio–Oyashio Extension region.

The Kuroshio along the ETC changes in time and space. Seasonally, the KT is strongest during summer and weakest during winter (Tang et al., 2000). During strong (weak) transport, the axis of the KT migrates seaward (shoreward), and less (more) Kuroshio Surface Water intrudes into the continental shelf of the southern ECS (Tang et al., 1999). Furthermore, observations indicate that the KT varies spatially from the eastern Philippines to north of the ETC Along the ETC, the meridional component of the KT is 9.1 Sv at 22°N and 20.6 Sv at 23°N. The accumulated KT along the ETC indicates that the northern branch of the North Equatorial Current (NEC) transport has a finite contribution to the KT variability there.

Eddy variability plays a substantial role on the KT. By comparing the volume transport at PCM-1 (black bold line in Fig. 2(a))

---

* Corresponding author. Address: Climate and Global Dynamics Division, National Center for Atmospheric Research, PO Box 3000, Boulder, CO 80307-3000, USA. Tel.: +1 303 4971346.

   E-mail address: ytseng@ucar.edu (Y.-H. Tseng).
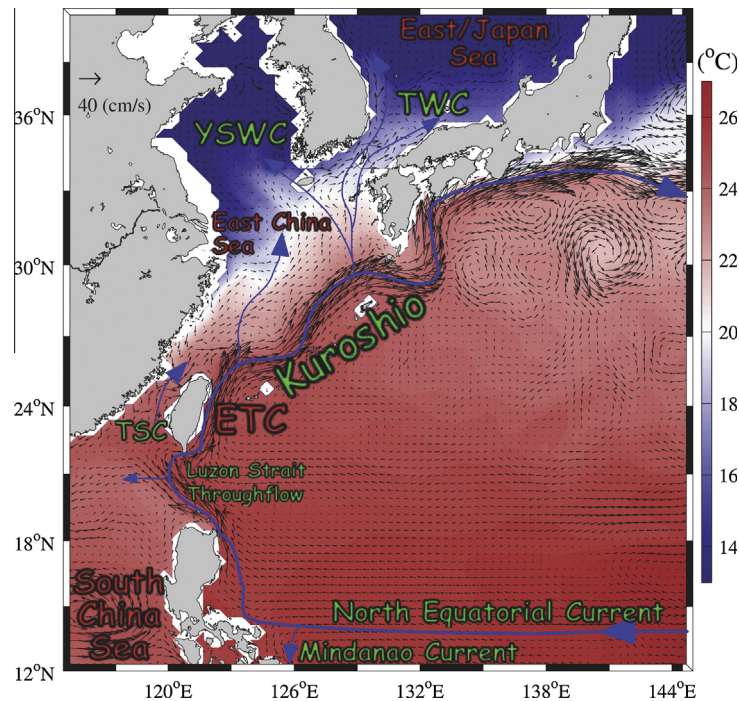[1] Present address: Hydrotech Research Institute, National Taiwan University, Taiwan.

Fig. 1. The main current system of western North Pacific, sketched as blue lines, including the North Equatorial Current (NEC), Kuroshio Current along the East Taiwan Channel (ETC), the Kuroshio Extension, Mindanao Current (MC), Taiwan Strait Current (TSC), Tushima Warm Current (TWC) and Yellow Sea Warm Current (YSWC). The modeled annual-averaged upper layer (above 50 m) velocity vectors and surface temperature are superimposed.

and the surrounding sea surface height (SSH), Zhang et al. (2001) suggests that the 100-day oscillation of the KT is due to westward-propagating eddies. Gilson and Roemmich (2002) discovered that the Kuroshio structure and transport are commonly changed by impinging eddies, indicating a substantial interaction between Kuroshio and eddies. However, obtaining the long-term KT from *in situ* and cruise measurements is difficult because there is usually insufficient data to separate the transient eddy contribution to the measured transport resulting from significant variability on a wide range of space and time scales. Thus, the purpose of this study is to provide a quantitative analysis of such variability, including long-term and climate effects, by combining observations with model results.

The lack of long-term Kuroshio observations led to a limited understanding of the climate impact on Kuroshio along the ETC and of the climate conveyed by Kuroshio. When Hwang and Kao (2002) used more than a decade of satellite altimetry data to estimate the KT, they found that while the KT near the Luzon Strait has a strong correlation with El Niño-Southern Oscillation (ENSO), the KT off northeastern Taiwan does not. The modeled results in Qu et al. (2004) also indicate that the KT offshore of eastern Philippines (NEC northern branch) is consistent with the SOI index. No direct impact of ENSO was observed, however, in the Kuroshio downstream region such as the KT along the ETC (Hwang and Kao, 2002) and the Kuroshio south of Japan. Furthermore, based on two specific cruises, Kashino et al. (2009) discovered that the KT in the eastern part of Luzon Strait does not correlate well with ENSO and that only the maximal current speed connects closely with tropical climate events; this finding was stronger in the La Niña phase (2008) than in the El Niño phase (late 2006). The result also indicates that tropical climate variability is not the prevailing signal of the KT along the ETC, at least for well-observed ENSO signals on the ocean surface. Our analysis does not address the question of whether deep tropical ocean dynamics may significantly affect the KT, although this is an intriguing issue in view of observed intense vertically stacked equatorial vortices having

alternating time mean zonal velocity jets (Firing, 1987). We infer that the big vertical mixing of water-mass properties is likely associated with vertical velocity connecting the zonal jets in the equatorial region, and that this may be related to Taylor–Couette-type centrifugal instabilities (Hua et al., 1997).

Moreover, the Tsushima warm current, a branch of the Kuroshio preceding the winter Western Pacific teleconnection pattern (Hirose et al., 2009), reveals the existence of ocean-to-atmosphere feedback and indicates that the Kuroshio may not be completely controlled by tropical circulations alone. The contribution from subtropical climate variability is indispensable but remains unclear. Because a long period of continuous observation is required to understand the long-term variability of the KT and its link with climate response, we used the SSH to estimate the KT of the PCM-1 line and its long-term variability. The SSH field can also be employed as an indicator of transport variability (Fukumori et al., 1996; Hirschi et al., 2009; Tierney et al., 2000; Vinogradova et al., 2007). The well-validated Duo-grids North Pacific Ocean model, DUPOM (Tseng et al., 2012), was utilized in this research to reveal relations between the *in situ* measured Kuroshio (Fig. 1) and satellite altimetry-based height differences between locations A and B (Fig. 2(a)) via three approaches: the geostrophic relationship (GR), the empirical relationship (ER), and the transfer function (TF).

The remainder of this paper is organized as follows: Section 2 describes the data and methods followed to construct the KT; Section 3 briefly describes the numerical model and a comparison of the long-term KT constructed by various approaches; Section 4 presents the constructed KT for the PCM-1 line and verifies the results; Section 5 discusses the climate variability conveyed by the KT along the ETC; and Section 6 offers conclusions.

2. Data and methods

The Sea Level Anomaly (SLA) field is introduced in Section 2.1. The three approaches used to construct the KT of PCM-1 (noted
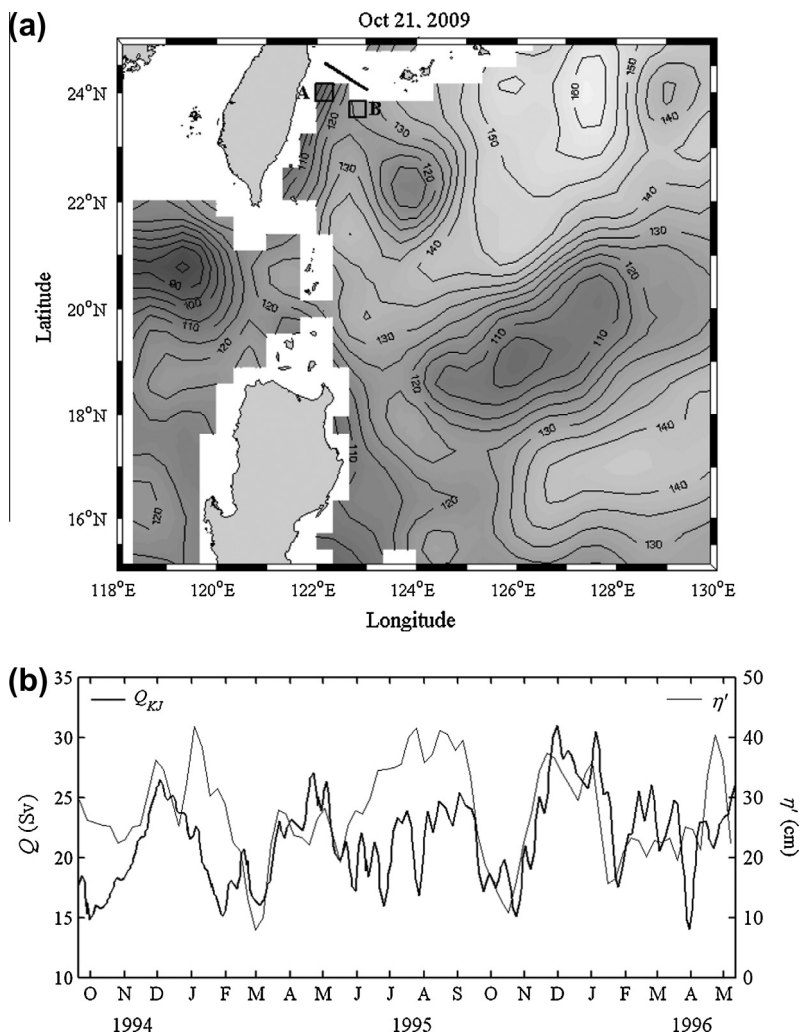
Fig. 2. (a) The SSH field on October 21, 2009, based on the mean sea surface height (SSH) and the sea level anomaly (SLA) (contour interval is 5 cm). The mean SSH is from the geodetic mean dynamic topography depth by Rio et al. (2009) and the SLA is from sea surface AVISO altimetry products. Depth less than 200 m is not shown. The Box A is chosen as the referenced SSH and the Box B was chosen so that the SSH difference (η') between Boxes A and B has the highest correlation with the KT on Section PCM-1 (black bold line). (b) Comparison of time series of Kuroshio Transport on the PCM-1 Section (Q_{KJ}, bold line) and η' (correlation is 0.40). The time series of Q_{KJ} contains more high frequency variability than that of η'. This is partially due to the different sampling-frequency of the WOCE PCM-1 observation and the Aviso SLA.

as Q_K) through the associated SSH difference are described in Sections 2.2 and 2.3.

2.1. Data description

The SLA was distributed by Aviso (http://www.aviso.ocea-nobs.com/). This dataset combines sea surface altimetry from Topex/Poseidon, ERS-1, ERS-2, Jason-1, and ENVISAT (depending on availability) into a product of merged SLA[1] which has a $1/3° \times 1/3°$ spatial resolution and a seven-day time interval. The SLA superimposed on the geodetic Mean Dynamic Topography (MDT) forms the SSH field in this study. The MDT is the hybrid mean performed by Rio et al. (2009) (hereafter referred to as Rio09). This MDT, also known as MDT CNES-CLS09, has a $1/4° \times 1/4°$ spatial resolution and combines the GRACE geoid, drifting buoy velocities, profiling float, and hydrographic temperature/salinity data.

A snapshot of the observed SSH field is shown in Fig. 2(a). The SSH field over bathymetry less than 200 m was not used because of possible residual tidal signals in shallow-water regions. The PCM-1 line is labeled as a bold black line. Approximations (proxies)

for the limited-duration, directly measured (*in situ*) transport through the PCM-1 line may be based on longer-term satellite altimetry data in the nearby upstream area of the PCM-1 line (see Section 2.2). These proxies were optimized using DUPOM model results and then used for transport through the PCM-1 line avoiding problems near the shallow edges of the PCM-1 line. We chose the area-averaged SSH of Box A, η_A, in Fig. 2(a) as a referenced low-SSH proxy. The SSH anomaly was calculated by subtracting η_A from the total SSH and then used to map its correlation with the observed KT in the PCM-1 line (Q_{KJ}), represented by the bold line in Fig. 2(b) (Johns et al., 2001). We selected the highest correlation area as a high-SSH proxy (Box B). The SSH difference between Box A and Box B, noted as η' (thin line in Fig. 2(b)), was used as the proxy of the cross-section height jump along the PCM-1 line. The observed Q_{KJ} was interpolated into a seven-day time interval for consistency. Not only does the line between these two boxes include the current core of the Kuroshio, which has a velocity maximum around 40–50 km offshore, but it covers the seasonal Kuroshio migration, which is in a range around $0.15°$ around the ETC (Tang et al., 2000). The steric effects were excluded because the span of PCM-1 is only $0.5°$ and the steric influence is limited. Furthermore, the comparison between Argo steric height and Aviso altimetry shows strong seasonal cycle and the

---

[1] Ssalto/Duacs User Handbook : (M)SLA and (M)ADT Near-Real Time and Delayed Time Products.

magnitude is approximately ±0.5 cm (Roemmich and Gilson, 2009). This indicates that the magnitude due to steric contribution is relatively small in the annual averaging sense compared to the SSH difference η', which is about 10–40 cm, as shown in Fig. 2(b).

Fig. 2(b) shows that the actual Q_{KJ} is roughly proportional to η' due to the barotropic transport of Kuroshio, although the baroclinic mode (coupled geostrophically to density gradients) is significant, resulting in much smaller Q_{KJ}. This implies that the transport associated with the subsurface geostrophic thermal wind (mostly negative in western boundary currents due to systematic density decrease with increasing distance from shore) is roughly proportional to the height difference.

The along-track altimetry data is more appropriate than the smoothed gridded one to accurately estimate the Kuroshio transport if its track spans the entire Kuroshio near the PCM-1 line. Unfortunately, no such long-track altimetry data exists; thus the present approach to optimize the A and B locations is reasonable and practical. We strategically selected the boxes with highest correlation to obtain the optimal statistical significance. Ivchenko et al. (2011) also demonstrated that the SSH can be used successfully to estimate oceanic transport variability if the seasonal thermocline variability is removed. Furthermore, we emphasized the interannual and long-term transport variability rather than daily- or monthly-based transport, which makes the SSH difference-estimated transport more meaningful.

2.2. Geostrophic relationship (GR) and empirical relationship (ER)

The inviscid momentum equations can be written as follows:

$$\rho \left[\frac{D\mathbf{u}}{Dt} + f\hat{\mathbf{z}} \times \mathbf{u} \right] = -\nabla p + \mathbf{F} \tag{1}$$

where $\mathbf{u}$ is the velocity vector, p is the pressure, $\mathbf{F}$ is surface forcing, t is the time, f is the Coriolis factor $f = 2\Omega \sin \phi$ ($\Omega = 7.292 \times 10^{-5}$ s^{-1}, ϕ is the latitude), and ρ is the density of fluid.

If the shallow-water and hydrostatic assumptions are applied and only the meridional transport is addressed, Eq. (1) can be reduced to the following equation:

$$f v = g \frac{\rho_o}{\rho} \frac{\partial \eta}{\partial x} + \left(\frac{F_x}{\rho} - \frac{Du}{Dt} \right) \tag{2}$$

where g is the acceleration of gravity, v is the meridional velocity, and F_x is the zonal boundary forcing.

By taking zonal integral and dividing by f, we have

$$Q = H \frac{g}{f} \frac{\rho_o}{\rho} \eta' + \frac{1}{f} \int \left(\frac{F_x}{\rho} - \frac{Du}{Dt} \right) H dx \tag{3}$$

where Q is the volume transport and H is the mean depth of the upper layer. For example, $H = 400$ m was used as the mean depth of the KT offshore of eastern Philippines (Qu et al., 1998).

This formula includes the geostrophic transport (the first term on the right side) and the ageostrophic one (the second term on the right side). The first term indicates the transport balanced by the pressure gradient and Coriolis force, and the second term represents the transport induced by the surface-forcing change, local acceleration, and convective acceleration.

The geostrophic balance relationship was used in the ocean to compute the volume transport of the upper layer based on height difference η' across the current, as follows:

$$Q_{kg} = H \frac{g}{f} \eta' \tag{4}$$

where Q_{Kg} is Q_K determined by the GR.

The GR was commonly applied to estimate the transport variability of the Kuroshio elsewhere, such as Luzon Strait, off northeastern Taiwan (Hwang and Kao, 2002), the East China Sea (Andres et al., 2008), and south of Japan (Imawaki et al., 2001).

A more realistic linear relation form than Eq. (4) for transport based on the GR can be constructed by comparing Q_K and η' (Andres et al., 2008):

$$Q_{Ke} = C_1 \eta' + C = H \frac{g}{f} \eta' + C \tag{5}$$

where Q_{Ke} is the Q_K constructed by the ER where C_1 and C are the coefficients calculated by the least square method or polynomial fit.

This linear relation may be rewritten as the superposition of the geostrophic part $\left(H \frac{g}{f} \eta' \right)$, which is the same as the first term on the right side of Eq. (3), and the ageostrophic part, which is the same as the second term on the right side of Eq. (3). However, H may not be the same for different realizations because the vertical structures in the ocean vary and the thermal wind transport may not be linearly proportional to η'; careful comparison is essential to interpret the results. Andres et al. (2008) showed that ER can be used successfully to estimate the KT in the East China Sea. This approach may also be useful to estimate the KT in the PCM-1 line.

Both H and C must be optimized to fit the available altimetry and direct transport measurements in the PCM-1 line. Here, the optimization was done based on a short period during which direct observation was performed (18 months in 1993–1996) and a 10-year model simulation, individually.

2.3. Transfer function (TF)

The frequency-dependent "transfer function" (TF) (Åström and Murray, 2008) estimates the linear causal relationship between any pair of variables and is a useful tool for linking Q_K and η', i.e., $Q_K(\omega) = T_{\eta Q}(\omega) \eta'(\omega)$, where $T_{\eta Q}$ is regarded as a "geostrophic coefficient" similar to Eq. (4) if the linear relation is held. However, other nonlinear terms may also be involved (see Appendix and the following description). The TF has been used to evaluate an ENSO model (MacMynowski and Tziperman, 2010) and to verify the bottom shear stress under surface waves (Shen, 2009; Shen and Huang, 2008).

The TF can be directly derived from the momentum equation and the associated relations for the Shallow-Water Equations (see Appendix for details), though the governing equations are not required in general. $T_{\eta Q}(\omega)$ is defined as follows:

$$T_{\eta Q}(\omega) = \frac{\widetilde{Q}_K(\omega)}{\tilde{\eta}'(\omega)} \tag{6}$$

where the tilde $\sim$ denotes the Fourier transform.

Thus Q_{Kt}, the Q_K established by the TF, can be defined as $Q_{Kt} = F^{-1}(T_{\eta Q} \tilde{\eta}')$, where F^{-1} is the operator of inverse Fourier transform. The possible nonlinear causal relationship between Q_K and η' must be considered when interpreting results based on TF. A typical nonlinear relationship is the interaction of the Kuroshio with complex bathymetry, which results in a countercurrent and thus changes the SSH field when the Kuroshio is passing the Ilan Ridge (Tang et al., 2000). The changes of both Q_K and η' may result from another environmental variable such as a regional variation of sea level pressure (raising the anomaly on SSH and the KT locally) or local wind variation (affecting Ekman transport as well as surface transport).

The standard deviation of the estimated TF amplitude bias (σ_A), according to Swanson (2000), is:

$$\sigma_A^2(\omega) = \frac{1}{2k} \frac{1 - \gamma_{\eta Q}^2(\omega)}{\gamma_{\eta Q}^2(\omega)} |T_{\eta Q}(\omega)|^2 \tag{7}$$

where $\gamma_{\eta Q}(\omega) = |S_{\eta Q}(\omega)|/\sqrt{S_{\eta\eta}(\omega)S_{QQ}(\omega)}$ is the coherence function for the associated spectral output, and k is the number of data segments.

The standard deviation of the estimated TF phase bias (σ_θ), according to Swanson (2000), is:

$$\sigma_\theta^2(\omega) = \tan^{-1}\left[\sqrt{\frac{1}{2k}\frac{1 - \gamma_{\eta Q}^2(\omega)}{\gamma_{\eta Q}^2(\omega)}}\right] \qquad (8)$$

The uncertainty in the estimated magnitude and phase of $T_{\eta Q}$ increases as the coherence of the two signals decreases, which may be due to the nonlinear casual relationship between Q_K and η', or as the number of segments decreases, which may require a longer observation period.

3. Evaluation of Kuroshio transport (KT) reconstruction using model results

The numerical model is an efficient tool to evaluate the long-term estimation of the KT. We briefly described our numerical model (Section 3.1) and investigated the reconstruction of Q_K through the modeled SSH difference η' (defined in Section 2.1). The transfer function $T_{\eta Q}$ (defined in Eq. (6)) and the coefficients of ER and GR were determined by 1-year model results Q_K and η'. The 10-year-modeled Kuroshio transport Q_K (noted as Q_M) was compared with the reconstructed Q_K to investigate the characteristics of various approaches.

3.1. Model description

We used the hydrostatic, z-level, mixed collocated Arakawa A and C grids and the fourth-order accurate DUPOM. The model uses fourth-order accuracy and provides low numerical dissipation and dispersion (Dietrich et al., 2004; Tseng et al., 2005). The DUPOM is currently a standard configuration of Taiwan Multiscale Community Ocean Model (TIMCOM) (Young et al., 2012), which is used to simulate a variety of ocean dynamics by the novel multiple-domain approach (Tseng et al., 2012).

The DUPOM domain covers the entire North Pacific Ocean ranging from 100°E to 80°W and 30°S to 60°N. Fig. 3 shows the model domain and the bathymetry. A duo-grid approach was used to reduce the computational time based on the multiple-grid frame-work (Dietrich et al., 2004, 2008). A 1/4° × 1/4° horizontal resolution was used east of 150°E (right block in Fig. 3, NPB domain), and a finer horizontal resolution of 1/8° × 1/8° was used west of 150°E (left block in Fig. 3, TAI domain), in which the Kuroshio and its associated circulations in the marginal seas are resolved accurately.

The model bathymetry is interpolated from unfiltered ETOPO-2 depth data supplemented with the one-minute, high-accuracy depth archive in the Asian Seas (Liu et al., 1998) from the National Center for Ocean Research (NCOR) of Taiwan. The vertical resolution is a linear-exponential stretched grid of 25 layers with a top layer thickness of 6 m. Both domains use the same vertical grids to avoid inconsistency. Within each domain, the longitudinal resolution is uniform and the latitudinal resolution is generated so that the varying latitude and longitude grid increments are equal everywhere (Mercator grid).

The surface wind forcing is obtained from the interpolated monthly Hellerman and Rosenstein winds stress (Hellerman and Rosenstein, 1983). The Levitus94 seasonal climatology (Levitus and Boyer, 1994) is used to initialize the model and determine its surface sources of heat and fresh water using the non-damping approach. Further details about the model set-up and description can be found in Tseng et al. (2010, 2012). Even though the DUPOM is driven by climatological forcing, the model still shows the interannual variability of the KT. The reason is that major interannual ocean dynamics occur due to the ocean's natural intrinsic variability—for example, the Gulf of Mexico general circulation is dominated by major Loop Current eddies whose dynamics are intrinsic to the fact that its internal dynamics have natural time scales related to interannual atmospheric variability or even seasonal cycles, as is clearly shown by modeling studies.

We compared the modeled annual-averaged SSH (Fig. 4(a)) and the Rio09 SSH field (Fig. 4(b)). The NEC bifurcation latitude is located at approximately 13.5°N in the modeled mean SSH, which is slightly north of that in Rio09 (at approximately 12°N). This contributes to a broader and weaker modeled Mindanao Current (MC) close to the southern boundary. However, the KT along the ETC and Okinawa Trough is consistent with Rio09, indicating a reliable modeled KT with an associated subtropical gyre and western boundary current system.

The mean modeled current structure east of Taiwan (PCM-1 line) during September in Year 37 to next May is shown in Fig. 4(c). The strong Kuroshio flows northeastward (positive value),
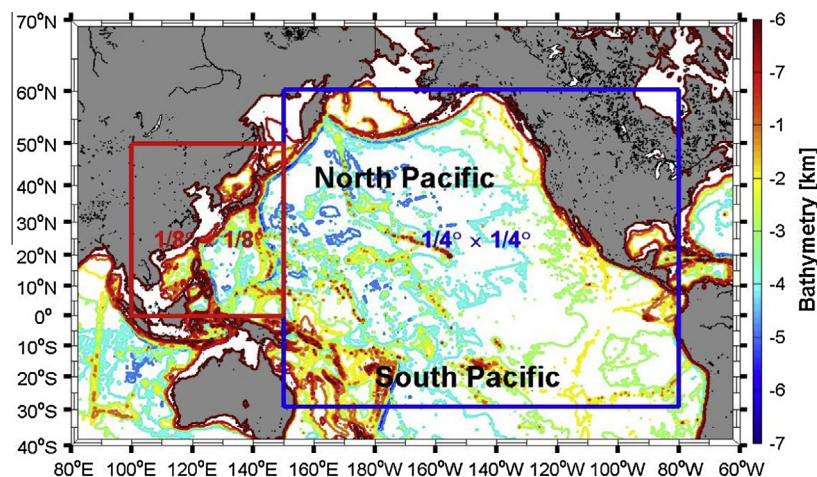

Fig. 3. Schematic of the DUPOM domain. The NPB domain (right block) covers the eastern Pacific with a horizontal grid resolution of 1/4° × 1/4°, while the TAI domain (left block) covers the western Pacific with a finer horizontal grid resolution of 1/8° × 1/8°. The contour interval of bathymetry is one kilometer.
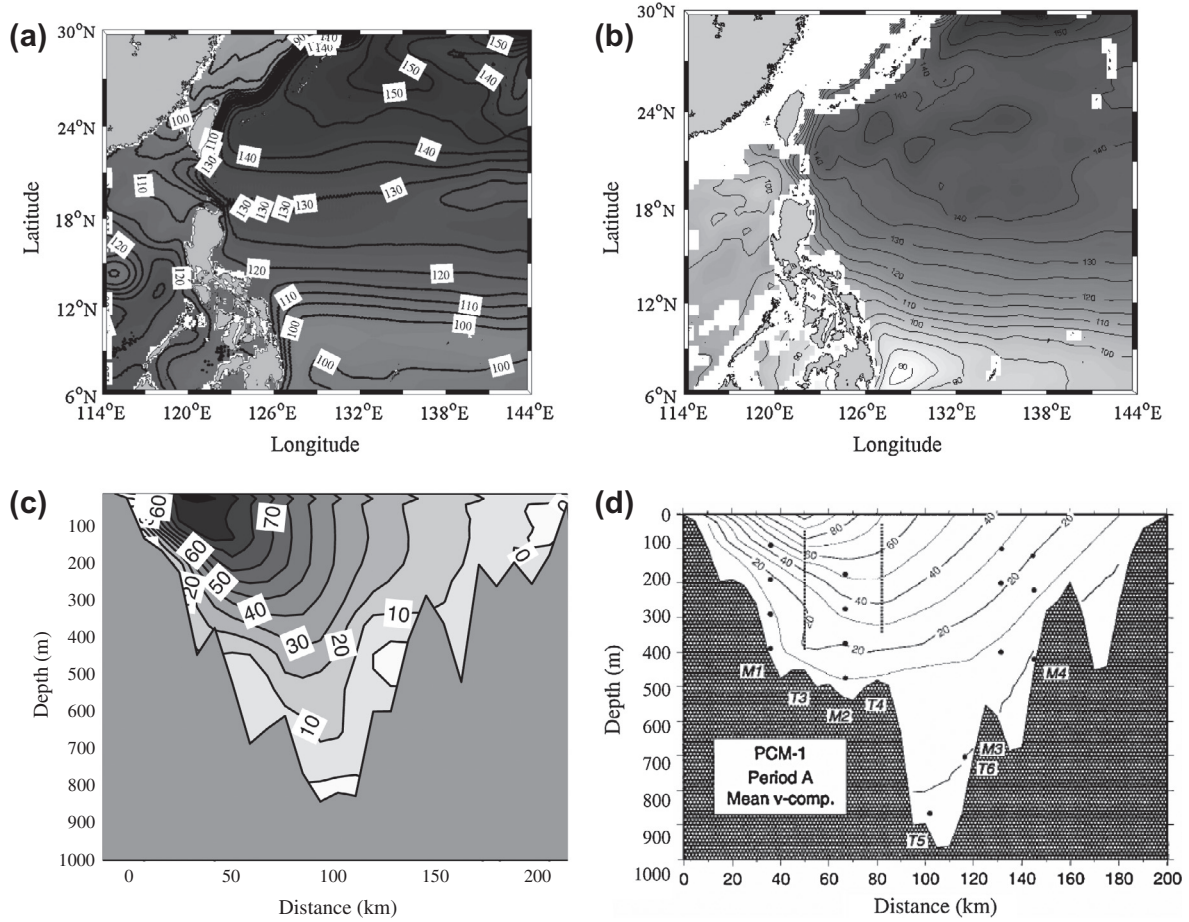
Fig. 4. (a) The modeled annual-averaged SSH field and (b) the mean SSH from Rio09 (depth less than 200 m is not shown). The contour interval is 10 cm. (c) The modeled annual-averaged cross-section velocity profile (Year 37 September to next May) and (d) the observation of PCM-1 during the period from September 1994 to May 1995 (Fig. 5 of Johns et al., 2001). The contour interval is 10 cm/s.

typically at a speed of over 50 cm/s. The current core has a maximal mean velocity of 102.3 cm/s at nearly 40–50 km offshore near 30 m deep. In general, this current structure is similar to the PCM-1 observation (Fig. 4(d)) for the period September 1994-May 1995 (Fig. 5 of Johns et al. (2001)). Further model validation can be found in Tseng et al. (2012). The good agreement of model results and observation suggests that the model dynamic is quite close to the real ocean dynamic.

3.2. The modeled characteristics of GR, ER, and TF reconstruction

Fig. 5 shows the relationship of Q_M and η' (solid dots) based on the model simulation of Year 38, measured from the same location as shown in Fig. 2(a). Both GR and ER relationships are compared in Fig. 5. The GR was determined by Eq. (4) and is shown as the bold line (H = 340 m). The comparison of GR with the Q_M–η' relationship indicates that the barotropic mode of geostrophic transport dominated the main features of modeled Q_K when η' was smaller than 22 cm. However, the GR failed when η' was larger than 22 cm. The Q_M–η' relationship departed from the GR, indicating that the lateral gradient, which typically decreases the velocity according to the geostrophic thermal wind relationship as one goes downward, is significant due to the strong KT.

The ER (thin line in Fig. 5) was determined using the least square method on Q_M and η' of Year 38, which may correlate optimally with the dataset. However, the reconstruction may mix the fast ageostrophic mode transport, transport due to lateral density
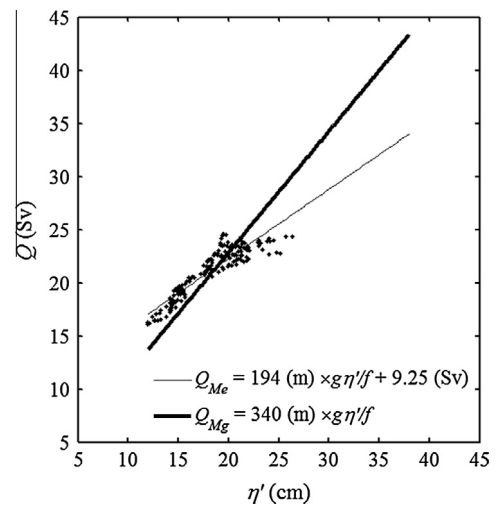

Fig. 5. Scatter plot of the modeled transport Q_M (solid dot) and the associated SSH difference η' in model Year 38, superimposed by the empirical relationship (ER, thin line) and the Geostrophic Relationship (GR, bold line) reconstruction. The good correlation of 0.91 suggests the pressure difference across the section, integrated vertically, gives a good estimate of the transport through the section according to the geostrophic approximation, and the η' is proportional to the near surface lateral pressure gradient according to the hydrostatic approximation. Therefore, the geostrophic and hydrostatic approximations are accurate for the purpose of calculating long-term KT.

gradient, and other nonlinear modes into an average transport. The formulae used in Fig. 5 separate the total transport into two contributions, with one contribution varying with η' and the other does not. The first term is the barotropic mode of geostrophic transport with the mean depth of upper layer $H = 194$ m; the second term can be regarded as the average of fast ageostrophic transport, nonlinear transport, or the transport excited by the lateral density gradient. The estimated H is shallower than 200 m, indicating that (i) the variability of Q_M is not entirely dominated by the geostrophic mode and may be carried by the seasonal thermocline layer (Hirschi et al., 2009), as well as influenced by the significant lateral density gradients, and (ii) the transport associated the subsurface geostrophic thermal wind is not proportional to η'. The ER-estimated KT indicates that these influences contribute to nearly half of the KT.

The amplitude and phase of $T_{\eta Q}$ based on the relationship of Q_M and its corresponding η' of the model Year 38 simulation are shown in Fig. 6(a) and (b), respectively. Theoretically, the barotropic mode of geostrophic transport is in proportion to η' and has no phase difference with η'; therefore, the response function remains constant (as noted in Eq. (4)), regardless of whether any frequency and latitude influence is negligible (that is, β-effect is insignificant). Fig. 6(a) indicates that the amplitude of low-frequency $T_{\eta Q}$ (period > 6 months) is approximately constant and has a near-zero
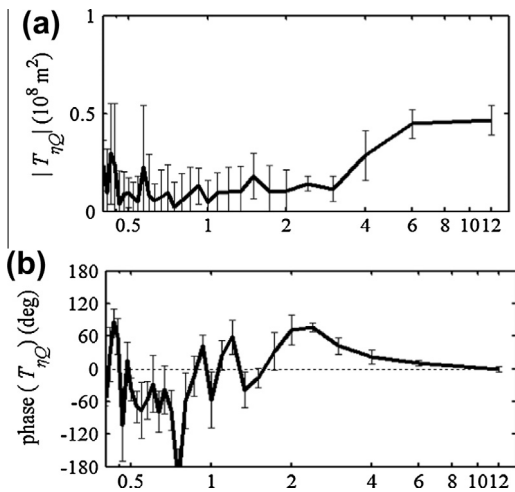

Fig. 6. The (a) amplitude and (b) phase of transfer function $T_{\eta Q}$ derived from model Year 38. The 95% confidence error bar is included to indicate the magnitude of uncertainty. The transfer function $T_{\eta Q}$ indicates frequency response (relation) of volume transport and the associated surface height difference, as defined in Eq. (6), see text for more discussion. For pure geostrophic flow, $T_{\eta Q}$ reduces to Hg/f, which is not a function of time, and there is no phase difference.

phase difference with small uncertainty, which indicates that the barotropic mode of geostrophic transport dominates these frequencies.

However, ageostrophic transport, flow due to seasonal lateral-density gradient change and nonlinear flow contributions, is evident for high-frequency band (period < 4 months), as indicated by the amplitude variation in Fig. 6(a) and the phase difference in Fig. 6(b). This indicates that no KT variability can be linked to variability in η' at subseasonal time scales. The ageostrophic component may result from the complex topography of the ETC or the lateral-density gradient becoming significant, which alters the current structures and incurs a nonlinear causal relation between Q_M and η'. The local wind field, which alters the short-term surface transport, may also play a key role. This behavior causes a larger uncertainty in capturing the variability of the KT using η' at short time scales. The exact mechanisms responsible for the phase difference are not clear. Thus, only the low-frequency variability of the KT, mainly the barotropic mode of geostrophic transport, can be efficiently established based on the link of Q_M and η'.

3.3. Long-term characteristics

For verification purposes, the three approaches described above were subsequently used to reconstruct the long-term variability of Q_M from η' in the model. The long-term modeled characteristics were investigated based on model Years 37–46. Fig. 7 compares the three-month running averaged KT (Q_M) with three surrogate KT approximations based on η', all derived from results of a 10-year simulation of the North Pacific Ocean by the DUPOM model. The actual Q_M (the solid line) exhibits seasonal variation, strong transport in the summer, and weak transport in the winter (consistent with the climatological view), and includes intrinsic interannual variability excited by major mesoscale eddies and basin scale oscillation.

The comparison of Q_M and Q_{Me} in Fig. 7 indicates that the ER-estimated Q_{Me} captured the averaged transport with a smaller variability. Specifically, the estimated Q_{Me} was consistent with the actual Q_M in early Year 40 and Years 41, 42, and 44, when the KT presented less variability. However, the estimated Q_{Me} was weaker than the actual Q_M in strong KT (e.g., Years 38 and 46), indicating that a number of energetic responses of oceanic transport are lost using the ER approach. Conversely, the variation of GR-estimated Q_{Mg} was larger than that of Q_M (the amplitude of Q_{Mg} was approximately 15 Sv, compared with only 10 Sv of the actual Q_M). Although the Q_{Mg} overpredicted the variation of the KT, it captured most of the Q_M variability, except for Year 43, in which a phase difference on seasonal cycle appeared. The Q_M in the late Year 43 decreased to 23 Sv and the Q_{Mg} increased to ~30 Sv. This phase difference resulted from the seasonal thermocline variation
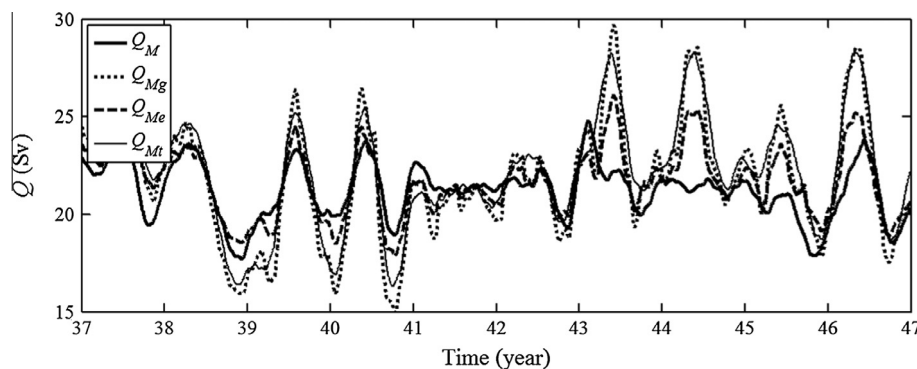

Fig. 7. Comparison of three-month running-averaged Q_M (bold solid lines) with three surrogate KT approximations based on η': GR (Q_{Mg}, dotted lines), ER (Q_{Me}, dashed lines) and TF (Q_{Mt}, thin lines).

(approximately upper 100 m), which was considerably influenced by the heat flux change on the ocean's surface (Ivchenko et al., 2011). The TF-estimated model transport (Q_{Mt}) efficiently captured the magnitude and the phase variance. This resulted in a better Q_{Mt} in Year 43 than Q_{Mg}. However, an exact reconstruction of phase and magnitude is not possible unless all modes within the frequency domains can be obtained.

Based on the 10-year model results, the transport of the upper 400 m are shown in Fig. 8 to identify the distinct stages of the KT as follows: (a) mean stage, and (b) strong flow stage (defined as the strong KT period, in which the transport was larger than one standard deviation). Bold lines indicate the contours of η_B, which were regarded as the eastern boundary of Kuroshio in the geostrophic view. The velocity vectors follow the SSH contours, regarded as the streamline in the long-term view.

In the mean stage (Fig. 8(a)), the modeled Kuroshio presents a similar pattern to the climatology. A comparison of the strong and mean flow stages in Fig. 8 may identify the possible origin of
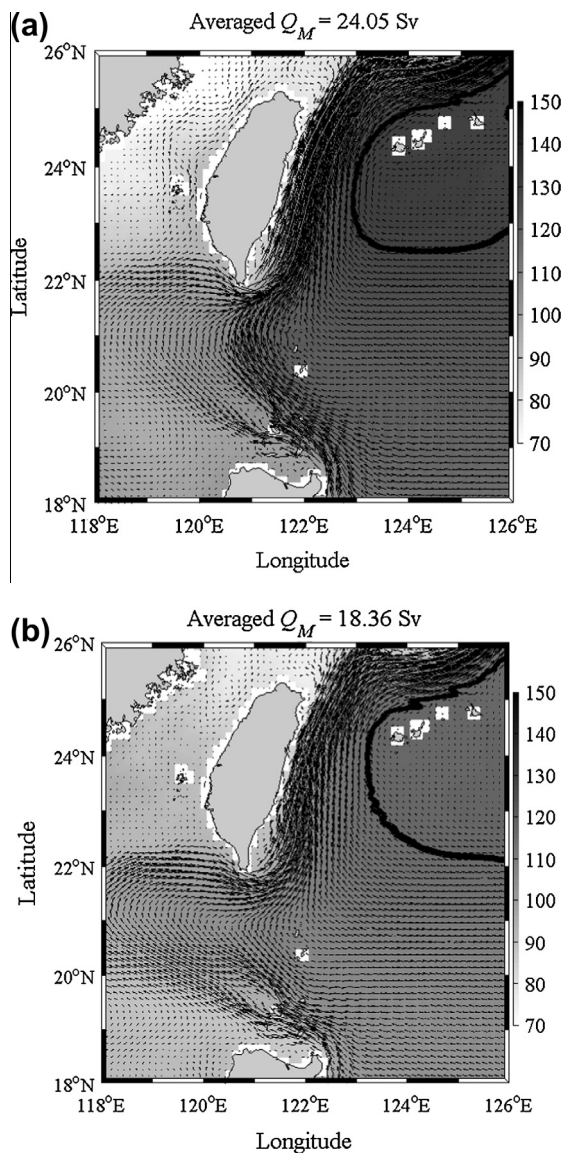
Q_M variability. We can see that the strong KT is associated with a stronger northern branch of NEC. Moreover, the interaction between Kuroshio and Luzon Strait Throughflow (LST) dominates the variation of Q_M. During the strong Q_M stage in Fig. 8(b), less LST intruded into the SCS and the Kuroshio flowed northward directly along a straighter path. More water mass was conveyed into the ETC than into SCS. This observation is supported by the eastern boundary of the Kuroshio in geostrophic view (the bold lines). A large amount of water mass originated from the subtropical gyre during the strong stage. Conversely, the LST was stronger and caused the Kuroshio to loop into SCS during the mean stage,which conveyed more Pacific water into the northern SCS.

4. Kuroshio transport (KT) reconstruction based on satellite altimetry

The long-term variability of actual Q_K was also reconstructed based on the observed η' measured using satellite altimetry, as described in Section 2. We understand that there is no robust approach to derive the actual Kuroshio transport; however, it is possible to infer the KT accurately from the satellite altimetry based on a database established by the model, whose modeled dynamics can capture all real ocean dynamics, including the SSH. Here, the observed Q_{KJ} in Fig. 2(b) was used to establish the Q_{KJ}–η' relationship in reality.

4.1. Establishing the relationship

The transport versus SSH-difference relationships of the three approaches are shown in Figs. 9 (as the dotted GR and ER) and 10 (as the dotted TF). The estimated $H = 234$ m in the GR approach is shallower than that estimated from models (340 m) in the geostrophic view. This may result from the phase difference between Q_{KJ} and η', the fast ageostrophic mode transport, and the interaction of current, complex bathymetry, change of lateral density gradient, and the seasonal monsoon change. The ER approach is omitted in the following discussion because the ER-estimated height is too shallow (53 m), indicating that the estimated transport cannot efficiently represent the energetic variability of the KT, which is consistent with that observed in Section 3.

Fig. 10 shows (a) the spectrum of observed Q_{KJ} and η', (b) amplitude, and (c) phase of transfer function $T_{\eta Q}$ (bold lines). The associated uncertainty is superimposed (in error bars). The two
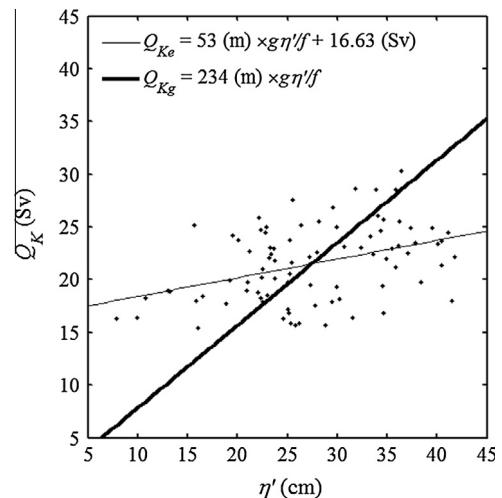

Fig. 8. The averaged upper layer (0–400 m) velocity vectors and SSH field (shaded) over (a) the modeled 10-year period and (b) the strong KT period, in which the transport was larger than one standard deviation. The bold line indicates the surface height contour considered to be the boundary of the Kuroshio Current (including its source from the North Equatorial Current region). The averaged transport during each period is labeled.

Fig. 9. Same as Fig. 5, but for the observation (the KT on the PCM-1 Section, Q_{KJ}). The correlation between actual Q_{KJ} and reconstructed Q_{Kg} is 0.39.
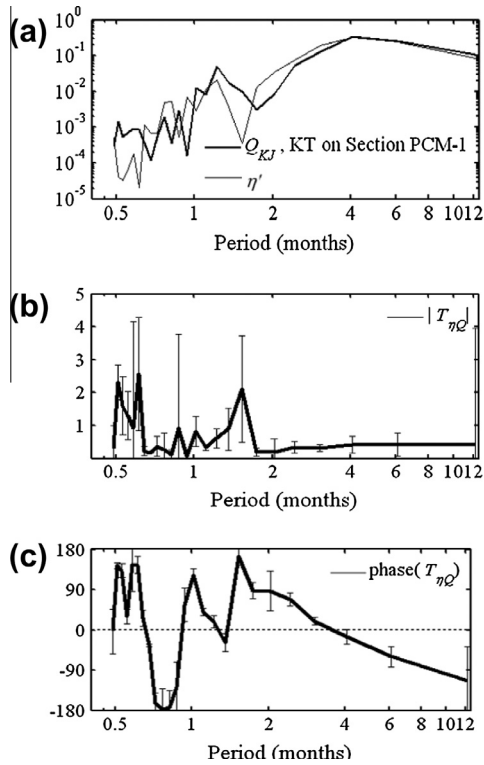
Fig. 10. (a) The spectrum of observed Q_{KJ} and η', (b) amplitude, and (c) phase of transfer function $T_{\eta Q}$. The associated uncertainty is superimposed (in error bars). The normalized spectra shows the major variability was dominated by the low frequency components, whereas the fast mode contributes little to the KT time averaged transport when the averaging is longer than a few months. This can also be seen in (b) that dramatic uncertainty and variability exist in the fast mode (0.5–2 month) and disappear automatically when averaging is longer than two months.
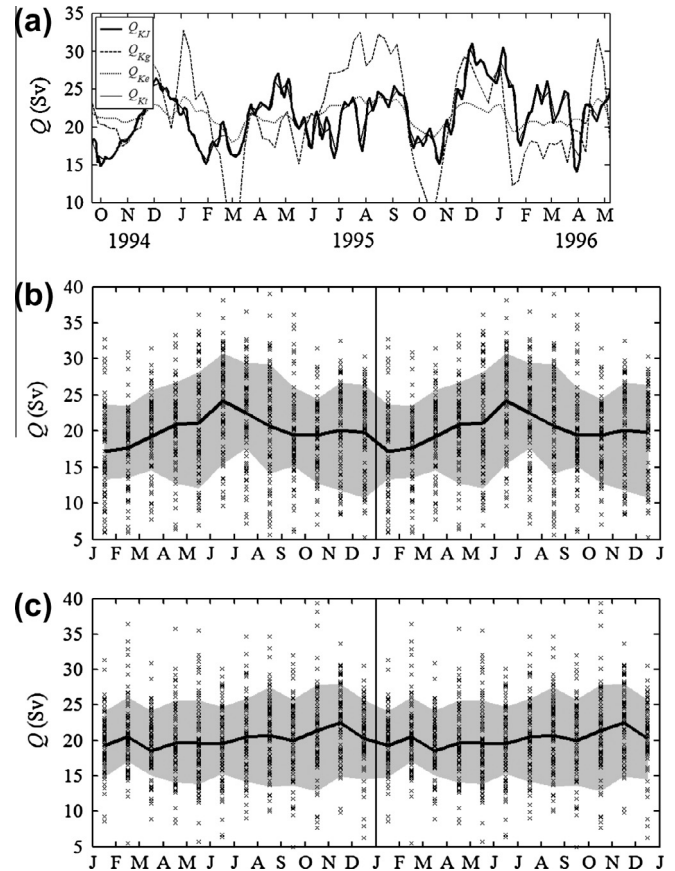

Fig. 11. (a) The reconstructed KT from 1994 to 1996 by various methods; the observed Q_{KJ} is also shown for comparison (bold solid line). (b) Monthly averaged Kuroshio transport estimated using GR, Q_{Kg} (dashed line), and its associated standard deviation range (shaded) as a function of calendar month. (c) Same as (b) but for Q_{Kt}. On each figure, x indicates individual transport each month. Results show the Q_{Kt} can well reconstruct the short term variability but cannot reproduce the well-known Kuroshio seasonal variability, whereas the Q_{Kg} can well reproduce the seasonal variability of Kuroshio and misses only the fast mode of Kuroshio.

dominant modes are the annual and seasonal cycles, which are consistent with observations (Johns et al., 2001). The low frequency $|T_{\eta Q}|$ (period > 4 months) is also close to a constant, indicating the prevailing geostrophic balance over the observation periods. The similarity of modeled and observed transfer function $T_{\eta Q}$ (comparing Fig. 6(a) with Fig. 10(b)) indicates that our numerical model efficiently captured the low-frequency response of η' due to the transport change. The high frequency $|T_{\eta Q}|$ (period < 3 - months) varies significantly between 0 and 2.5, indicating some short time-scale effects such as local winds, bathymetry-induced flow, as well as the fast ageostrophic component. The high-frequency response of the modeled $|T_{\eta Q}|$ is relatively weaker than that of observation, indicating that some subseasonal, high-frequency modes are not effectively resolved in the numerical model because of repeated climatological winds.

The relationship of Q_{KJ} and η' has no phase difference under geostrophic balance; thus, the phase of $|T_{\eta Q}|$ should be zero. However, the phase of $|T_{\eta Q}|$ in Fig. 10(c) indicates a large deviation in low frequencies (>4 months). The small uncertainty of $T_{\eta Q}$ occurs only for the periods of 2 to 6 months because of the 7-day observational time interval and the limited 20-month observational period. A large uncertainty was observed in both amplitude and phase near the annual cycle, indicating that the reconstructed Q_K using $T_{\eta Q}$ may be unable to reconstruct the long-term realistic KT.

4.2. The reconstructed Q_K of 1993–2010

The reconstructed Q_K using various methods is compared with Q_{KJ} (solid bold line) in Fig. 11(a), with the associated η'. The consistency between Q_{KJ} and TF-estimated transport Q_{Kt} was expected

because their relationship was directly established by the transfer function $T_{\eta Q}$. The GR-estimated transport Q_{Kg} mainly follows the low-frequency variation of η' and was not affected by the low correlation of Q_{KJ}–η'. This indicates that the Q_{Kg} captures only the barotropic mode of geostrophic Kuroshio transport. Our analysis indicates that both the TF and GR can provide reliable short-term variability with various characteristics.

The seasonal patterns of Q_{Kg} and Q_{Kt} (Fig. 11(b) and (c)) were examined based on two repeated cycles. The annual Q_{Kg} was approximately 20 ± 2 Sv. As suggested by Gilson and Roemmich (2002), the fluctuation was smaller than ±4 Sv. Consistent with earlier studies, January has the weakest Kuroshio transport, whereas June and July have the strongest transport. The annual Q_{Kt} exhibited a similar mean transport; however, the fluctuation was smaller (20 ± 0.5 Sv). The timing of extreme transport was not consistent with the earlier observation because of the uncertainty of the annual cycle in $T_{\eta Q}$. This is consistent with the previous discussion of $T_{\eta Q}$, where the $T_{\eta Q}$ was unable to construct the long-term variability unless a longer observation period (>2 years) was used. Thus, only Q_{Kg} was used to discuss the long-term KT in the next section.

5. Climate variability conveyed by the KT

This section presents verification of the long-term KT variability and its link with the North Pacific climate pattern. Because of its

geographical location, Q_K may originate from the northern branch of the NEC transport (Kuroshio upstream), the mesoscale eddy field (mainly resulting from westward-propagating Rossby waves), and the recirculation separated off southern Japan (Kuroshio downstream). These results indicate that both tropical and extratropical (mid-latitude) climate patterns may affect the variability of Kuroshio at various time scales. In the tropics, the dominant tropical climate forcing is ENSO (Qiu and Chen, 2010a; Solomon, 2010; Wang and Hu, 2006). In the mid-latitude, the WP pattern controls the major mid-latitude winter variability and connects with the eddy strengths generated from the SubTropical CounterCurrent (STCC) (Qiu and Chen, 2010b). We further analyzed the link of ENSO and WP signals with the reconstructed Kuroshio transport east of Taiwan.

5.1. Time series correlations

We compared the anomaly of a 13-month running mean of Q_{Kg} with ENSO (Niño 3.4) and WP indices to investigate the long-term variability of the KT (Fig. 12(a)) since 1993. Both indices are distributed by the NOAA Climate Prediction Center (http://www.cpc.ncep.noaa.gov). The cross-correlations of Q_{Kg} and these climate signals are also shown in Fig. 12(b). The lag between ENSO and Q_{Kg} may result from tropical Rossby waves, which carry the interaction of tradewind variability and tropical hydrographic features to the western Pacific and its marginal seas (Cai and He, 2010; Qu et al., 2004). The recharge paradigm for ENSO can explain the variability of NEC and thus the upstream of the KT. The highest correlation of Q_{Kg} and the ENSO index has a lag of two to four months; the highest correlation of Q_{Kg} and the WP index has a lag of nine months.

Note that the lag time may vary with the time period we choose, which indicates the non-stationary features of WP and ENSO indices (Tzeng et al., 2012). Nevertheless, the cross-correlation shows the existence of a certain time lag between the KT and these climate indices. No previous studies quantify and report the volume transport contribution from both the tropical and subtropical Pacific. Therefore, based on the volume transport contribution ratio in the well-validated DUPOM, we specify the same contributing ratio (0.455/0.545 for tropical/subtropical Pacific) to the observed KT. This weighting ratio led us to derive a combined time-series based on ENSO and WP indices as shown in the following:

$$Hyb_i = \alpha ENSO_{i-4} + (1 - \alpha)(-WP_{i-9}) \tag{9}$$

where Hyb is the hybrid signal in Fig. 12(a); i is the month; 4 and 9 are the phase lags for the ENSO and WP signal propagating to ETC, respectively; and α is the contributing ratio of KT volume transport from the tropical Pacific.

A considerably higher and significant correlation ($\sim$0.7) was obtained using this combined time series. The lag between the KT and WP indices is also consistent with Qiu and Chen (2010b), which suggests a nine-month delay for the STCC eddy field to adjust its meridional temperature gradient and the shear field in the response of WP variability. The STCC eddy field may accumulate the KT or pass through the LS into the SCS because of its broad meridional extent. The negative cross-correlation between Q_{Kg} and the WP index indicates that the nine-to-ten-month lag of Q_{Kg} is due to the STCC eddy field in the direct response of the WP pattern.
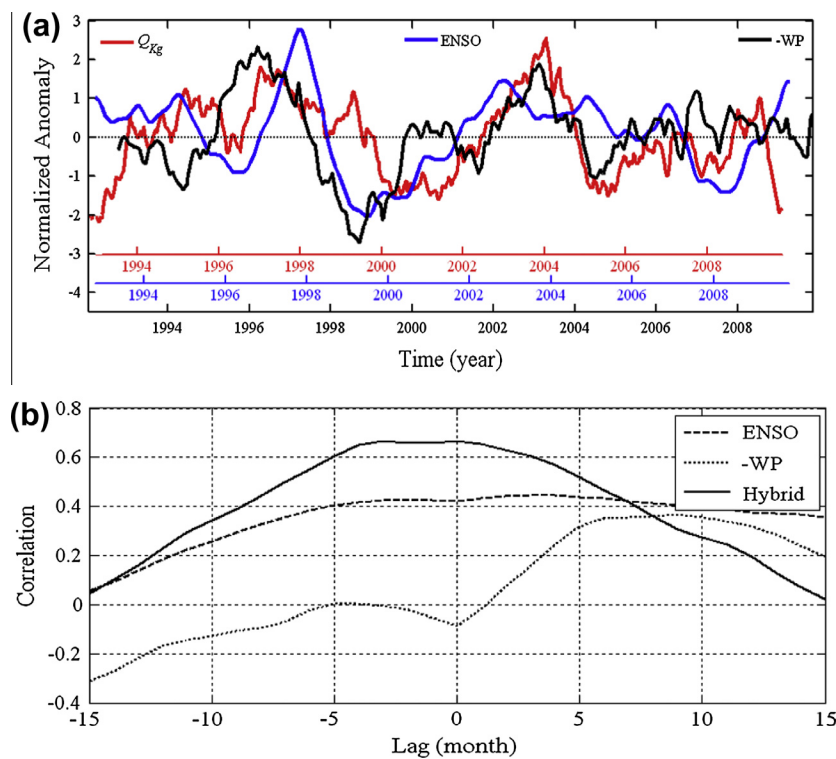

Fig. 12. (a) Comparison of 13-month running mean anomaly of Q_{Kg} with two climate indices: ENSO index (Niño 3.4; shown as blue) and negative WP index (shown as black). Note that the axis is shifted to take the lag into account. (b) The cross-correlation of Q_{Kg} and the two climate indices: ENSO and negative WP. The highest correlation of Q_{Kg} and ENSO index has a lag of 2–4 months while the highest correlation of Q_{Kg} and negative WP index has a lag of nine months. The hybrid signal is derived by combing the ENSO index and the negative WP index together. The better correlation indicates that the KT is impacted by tropical and subtropical climate dynamics. (For interpretation of the references to color in this figure legend, the reader is referred to the web version of this article.)

5.2. The strength of Kuroshio and its surrounding SSH variation

To further quantify the source of the KT variability and its associated role in the North Pacific climate, Fig. 13 shows the comparison of the mean SSH field in 1993–2010 and its standard deviation around Taiwan from three different stages: the average state, the strong transport period (averaged over the period during which the KT is larger than the mean plus its standard deviation,
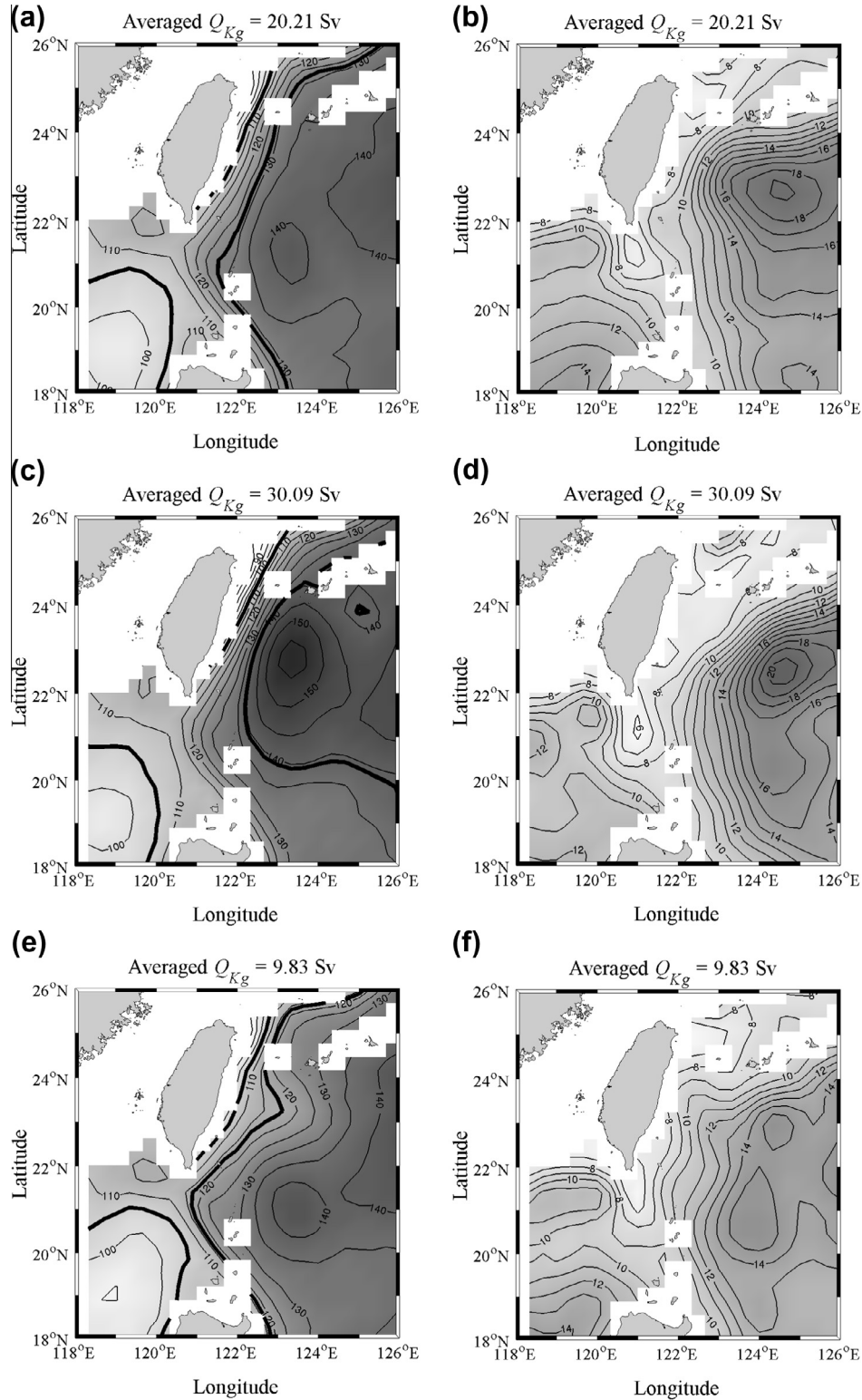

Fig. 13. The comparison of mean SSH field in 1993–2010 (left panels) and its standard deviation (right panels) around Taiwan from three different stages. (a) and (b) are the average state; (c) and (d) are the strong transport period (averaged over the period in which $Q_{kg} > \bar{Q}_{kg} + \sigma_Q$); and (e) and (f) are the weak transport period (averaged over the period in which $Q_{kg} < \bar{Q}_{kg} - \sigma_Q$). The bold contours of η_B were included to address the eastern boundary of the KT geostrophically.

$Q_{kg} > \bar{Q}_{kg} + \sigma_Q$), and the weak transport period (averaged over the period during which the KT is weaker than the mean minus its standard deviation $Q_{kg} < \bar{Q}_{kg} - \sigma_Q$). The averaged SSH contours (similar to the stream function) show the upper-layer ocean transport in geostrophic balance. The bold contours of η_B were included to address the eastern boundary of the KT geostrophically. The standard deviation of the SSH field shows the eddy strength statistically; the larger standard deviation indicates an eddy-rich and energetic region.

On average, Fig. 13(a) shows that the Kuroshio branches from the northern NEC and flows northward to the ETC, and subsequently northeastward into the Okinawa Trough. An anti-cyclonic eddy was commonly observed (Yang et al., 1999; Zhang et al., 2001) at approximately 124°E and 23.5°N east of the KT boundary (bold line). The high standard deviation region in Fig. 13(b), ranging from the Luzon Strait to the Ryukyu Islands, indicates the strong STCC eddy field east of Taiwan, and most of it merges into the Kuroshio along the ETC. Only a part of the eddies passes through the Luzon Strait and interacts with the Kuroshio (Zhang et al., 2001).

Fig. 13(c) and (e) shows the SST field during the strong and weak transport periods, respectively. A comparison of the eastern boundary of the KT (bold lines) in these figures indicates that more (or less) water mass originates from the NEC northern branch during the strong (or weak) KT period (approximately 25 cm and 10 cm SSH difference in (c) and (e), respectively). These results confirm the direct influence of the northern branch of NEC on the KT. However, the eddy fields exhibit a different variability of KT. During the average and strong KT period, an eddy-rich (high standard deviation) region was located at approximately 124.5°E and 22.5°N, indicating that more water mass from the eddies contributed into the KT along the ETC. During the weak KT period, the highest standard deviation core was located at approximately 124°E and 20.5°N at the entrance of the Luzon Strait and indicated that the eddies passed through the Luzon Strait into the SCS. This is consistent with the observation of He et al. (2010). The SSH field in SCS exhibited a minor difference among these three periods; however, the standard deviation varied considerably and indicated an energetic eddy field in the weak KT period (up to 14 cm in northern SCS at approximately 119°E and 21°N).

6. Conclusions

The GR, ER, and TF approaches were applied to reconstruct the variation of KT in the PCM-1 line. The modeled results were initially used to verify their characteristics. The reconstructed KT approximated by GR and TF is consistent with the modeled 10-year KT. Using a longer period of observation data, the TF provided a meaningful relationship between the KT and the associated SSH difference with less uncertainty than the other two approaches. But the GR can be applied successfully if targeted at low frequency variation (longer than four months), and is efficient in determining the long-term KT variability.

Our analysis indicated that two major sources directly affect the variability of the KT: the northern branch of the NEC transport and the STCC eddy field. The northern branch of the NEC transport can be easily detected from the temporal-averaged SSH field, in which the contour η_B from the NEC region indicates that the northern branch of the NEC transport contributes to the KT geostrophically. The STCC eddy field can be observed from the standard deviation field of the SSH, which indicates that the energetic eddy propagation introduces the high frequency (shorter time scale) variation of the KT and merges the STCC variability into the KT long-term variability. These results further confirm that both ENSO (conveyed by the NEC)

and WP (conveyed by the eddy fields east of Taiwan) patterns affect the variability of the KT at various time scales, and the correlation can be as high as 0.7 when both influences are considered. Further investigation on the mechanisms is ongoing and beyond the scope of this paper.

Appendix A

Non-dimensionalized momentum equations of the shallow-water can be written by the following asymptotic approximation, the Rossby number $\varepsilon = R_o \to 0$, the Burger number $\Gamma = (R_o/Fr)^2 = O(1)$ (McWilliams, 2006, p. 152).

$$\varepsilon \frac{D\mathbf{u}}{Dt} + f \cdot \hat{\mathbf{z}} \times \mathbf{u} = -\nabla p + \varepsilon \mathbf{F} \tag{A.1}$$

$$p = \Gamma \eta, \quad h = 1 + \varepsilon(\eta - B) \tag{A.2}$$

$$\varepsilon \frac{\partial \eta}{\partial t} + \varepsilon \nabla \cdot [(\eta - B)\mathbf{u}] = -\nabla \cdot \mathbf{u} \tag{A.3}$$

where Fr is the Froude number, $\mathbf{u}$ is the velocity vector, p is the pressure, $\mathbf{F}$ is the forcing from boundary, η is the surface height, B is the bathymetry depth, t is the time. In general, the dependent variables $\mathbf{u}$, η, p, and f can be expanded by ε using perturbation method. Namely,

$$\mathbf{u} = \mathbf{u}_o + \varepsilon \mathbf{u}_1 + \varepsilon^2 \mathbf{u}_2 + \cdots, \quad \eta = \eta_o + \varepsilon \eta_1 + \varepsilon^2 \eta_2 + \cdots \tag{A.4}$$

$$p = p_o + \varepsilon p_1 + \varepsilon^2 p_2 + \cdots, \quad f = f_o + \varepsilon f_1 + \varepsilon^2 f_2 + \cdots \tag{A.5}$$

The leading order term of the momentum equation $O(1)$ suggests geostrophic balance and the associated form as follows.

$$\hat{\mathbf{z}} \times \mathbf{u}_o = -\Gamma \nabla \eta_o \tag{A.6}$$

$$\nabla \cdot \mathbf{u}_o = 0, \quad \psi = \Gamma \eta_o \tag{A.7}$$

$$\mathbf{u}_o = \nabla \times \psi = \nabla \times (\Gamma \eta'_o) = \Gamma \delta \eta_o \delta \mathbf{x}^{-1} = \Re_{oo} \eta'_o, \quad \Re_{oo}$$
$$= \Gamma \delta \mathbf{x}^{-1} \tag{A.8}$$

Eq. (A.7) indicates the geostrophic flow is proportional to the surface height jump. The $O(\varepsilon)$ term balance can be written as follows.

$$\hat{\mathbf{z}} \times \mathbf{u}_1 = -\frac{D\mathbf{u}_o}{Dt} - \beta y \hat{\mathbf{z}} \times \mathbf{u}_o - \nabla \Gamma \eta_1 + \mathbf{F} \tag{A.9}$$

$$\nabla \cdot \mathbf{u}_1 = -\frac{\partial \eta_o}{\partial t} - \nabla \cdot [(\eta_o - B)\mathbf{u}_o] \tag{A.10}$$

$$\mathbf{u}_1 = \Re_{1o} \eta_o + \Re_{11} \eta_1 \tag{A.11}$$

Thus,

$$Q_K = \mathbf{u} \cdot \mathbf{A} = (\mathbf{u}_o + \varepsilon \mathbf{u}_1 + \varepsilon^2 \mathbf{u}_2 + \cdots) \cdot \mathbf{A}$$
$$= A(\Re_{oo} \eta_o + \varepsilon(\Re_{1o} \eta_o + \Re_{11} \eta_1) + \varepsilon^2 (\Re_{2o} \eta_o + \Re_{21} \eta_1$$
$$+ \Re_{22} \eta_2) + \cdots)$$
$$= A(a_o \eta_o + \varepsilon a_1 \eta_1 + \varepsilon^2 a_2 \eta_2 + \cdots)$$
$$\approx T_{\eta Q}(\eta_o + \varepsilon \eta_1 + \varepsilon^2 \eta_2 + \cdots) = T_{\eta Q} \eta \tag{A.12}$$

and agrees with $\varepsilon^n(T_{\eta Q} - Aa_n) \to 0$ for $n = 0, 1, 2, 3, \ldots$. By taking the Fourier transform with a frequency ω, we have

$$T_{\eta Q}(\omega) = \frac{\tilde{Q}_K(\omega)}{\tilde{\eta}'(\omega)} \tag{A.13}$$

The frequency-dependent TF is based on the relation of input and output, which are not required to be known in advance. The TF can be obtained from the time series of two signals.

References

Akitomo, K., Ooi, M., Awaji, T., Kutsuwada, K., 1996. Interannual variability of the Kuroshio transport in response to the wind stress field over the North Pacific: its relation to the path variation south of Japan. Journal of Geophysical Research 101, 14057–14071.

Andres, M., Park, J.-H., Wimbush, M., Zhu, X.-H., Chang, K.-I., Ichikawa, H., 2008. Study of the Kuroshio/Ryukyu Current system based on satellite-altimeter and *in situ* measurements. Journal of Oceanography 64, 937–950.

Åström, K.J., Murray, R.M., 2008. Feedback Systems: An Introduction for Scientists and Engineers. Princeton University Press, 424 pp.

Cai, S., He, Y., 2010. Association of the Sulu Sea surface circulation with the South China Sea. Journal of Marine Systems 81, 335–340.

Caruso, M., Gawarkiewicz, G., Beardsley, R., 2006. Interannual variability of the Kuroshio intrusion in the South China Sea. Journal of Oceanography 62, 559–575.

Centurioni, L.R., Niiler, P.P., Lee, D.-K., 2004. Observations of inflow of Philippine Sea surface water into the South China Sea through the Luzon Strait. Journal of Physical Oceanography 34, 113–121.

Chen, C.-T.A., 2005. Tracing tropical and intermediate waters from the South China Sea to the Okinawa Trough and beyond. Journal of Geophysical Research 110, C05012.

Chen, C.-T.A., 2008. Distributions of nutrients in the East China Sea and the South China Sea connection. Journal of Oceanography 64, 737–751.

Chen, C.-T.A., Sheu, D.D., 2006. Does the Taiwan Warm Current originate in the Taiwan Strait in wintertime? Journal of Geophysical Research 111, C04005.

Chen, C.-T.A., Ruo, R., Paid, S.-C., Liu, C.-T., Wong, G.T.F., 1995. Exchange of water masses between the East China Sea and the Kuroshio off northeastern Taiwan. Continental Shelf Research 15, 19–39.

Chern, C.-S., Jan, S., Wang, J., 2010. Numerical study of mean flow patterns in the South China Sea and the Luzon Strait. Ocean Dynamics 60, 1–13.

Dietrich, D.E., Mehra, A., Haney, R.L., Bowman, M.J., Tseng, Y.H., 2004. Dissipation effects in North Atlantic Ocean modeling. Geophysical Research Letters 31, L05302.

Dietrich, D.E. et al., 2008. Mediterranean Overflow Water (MOW) simulation using a coupled multiple-grid Mediterranean Sea/North Atlantic Ocean model. Journal of Geophysical Research 113, C07027.

Firing, E., 1987. Deep zonal currents in the central equatorial Pacific. Journal of Marine Research 45, 791–812.

Fukumori, I., Raghunath, R., Fu, L.L., 1996. The nature of global large-scale sea level variability in relation to atmospheric forcing: a modeling study. Journal of Geophysical Research 103, 5493–5512.

Gilson, J., Roemmich, D., 2002. Mean and temporal variability in Kuroshio geostrophic transport south of Taiwan (1993–2001). Journal of Oceanography 58, 183–195.

He, Y., Cai, S., Wang, S., 2010. The correlation of the surface circulation between the Western Pacific and the South China Sea from satellite altimetry data. International Journal of Remote Sensing 31, 4757–4778.

Hellerman, S., Rosenstein, M., 1983. Normal monthly wind stress over the world ocean with error estimates. Journal of Physical Oceanography 13, 1093–1104.

Hirose, N., Nishimura, K., Yamamoto, M., 2009. Observational evidence of a warm ocean current preceding a winter teleconnection pattern in the northwestern Pacific. Geophysical Research Letters 36, L09705.

Hirschi, J.J.M., Killworth, P.D., Blundell, J.R., Cromwell, D., 2009. Sea surface height signals as indicators for oceanic meridional mass transports. Journal of Physical Oceanography 39, 581–601.

Hu, J., Kawamura, H., Hong, H., Qi, Y., 2000. A review on the currents in the South China Sea: seasonal circulation, South China Sea warm current and Kuroshio intrusion. Journal of Oceanography 56, 607–624.

Hu, J., Kawamura, H., Li, C., Hong, H., Jiang, Y., 2010. Review on current and seawater volume transport through the Taiwan Strait. Journal of Oceanography 66, 591–610.

Hua, B.L., Le Gentil, S., Orlandi, P., 1997. First transitions in circular Couette flow with axial stratification. Physics of Fluids 9, 365–375.

Hwang, C., Kao, R., 2002. TOPEX/POSEIDON-derived space–time variations of the Kuroshio Current: applications of a gravimetric geoid and wavelet analysis. Geophysical Journal International 151, 835–847.

Imawaki, S., Uchida, H., Ichikawa, H., Fukasawa, M., Umatani, S., ASUKA Group, 2001. Satellite altimeter monitoring the Kuroshio Transport south of Japan. Geophysical Research Letters 28, 17–20.

Ivchenko, V.O., Sidorenko, D., Danilov, S., Losch, M., Schröter, J., 2011. Can sea surface height be used to estimate oceanic transport variability? Geophysical Research Letters 38, L11601.

Jan, S., Tseng, Y.-H., Dietrich, D., 2010. Sources of water in the Taiwan Strait. Journal of Oceanography 66, 211–221.

Johns, W.E., Lee, T.N., Zhang, D., Zantopp, R., Liu, C.-T., Yang, Y., 2001. The Kuroshio east of Taiwan: moored transport observations from the WOCE PCM-1 array. Journal of Physical Oceanography 31, 1031–1053.

Kashino, Y., España, N., Syamsudin, F., Richards, K., Jensen, T., Dutrieux, P., Ishida, A., 2009. Observations of the North Equatorial current, Mindanao current, and Kuroshio current system during the 2006/07 El Niño and 2007/08 La Niña. Journal of Oceanography 65, 325–333.

Kwon, Y.-O., Alexander, M.A., Bond, N.A., Frankignoul, C., Nakamura, H., Qiu, B., Thompson, L.A., 2010. Role of the Gulf Stream and Kuroshio–Oyashio systems in large-scale atmosphere–ocean interaction: a review. Journal of Climate 23, 3249–3281.

Lee, J.-S., Takeshi, M., 2007. Intrusion of Kuroshio water onto the continental shelf of the East China Sea. Journal of Oceanography 63, 309–325.

Levitus, S., Boyer, T.P., 1994. Temperature. World Ocean Atlas, 1994, vol. 4. NOAA Atlas NESDIS, 117 pp.

Liu, C.-S., Liu, S.-Y., Lallemand, S.E., Lundberg, N., Reed, D.L., 1998. Digital elevation model offshore Taiwan and its tectonic implications. Terrestrial Atmospheric and Oceanic Sciences 9, 705–738.

Ma, C., Wu, D., Lin, X., Yang, J., Ju, X., 2010. An open-ocean forcing in the East China and Yellow seas. Journal of Geophysical Research 115, C12056.

MacMynowski, D.G., Tziperman, E., 2010. Testing and improving ENSO models by process using transfer functions. Geophysical Research Letters 37, L19701.

Matsuno, T., Lee, J.S., Yanao, S., 2009. The Kuroshio exchange with the South and East China Seas. Ocean Science 5, 303–312.

McWilliams, J.C., 2006. Fundamentals of Geophysical Fluid Dynamics. Cambridge University Press.

Qiu, B., Chen, S., 2010a. Interannual-to-decadal variability in the bifurcation of the North Equatorial current off the Philippines. Journal of Physical Oceanography 40, 2525–2538.

Qiu, B., Chen, S., 2010b. Interannual variability of the North Pacific Subtropical Countercurrent and its associated mesoscale eddy field. Journal of Physical Oceanography 40, 213–225.

Qu, T., Mitsudera, H., Yamagata, T., 1998. On the western boundary currents in the Philippine Sea. Journal of Geophysical Research 103, 7537–7548.

Qu, T., Kim, Y.Y., Yaremchuk, M., Tozuka, T., Ishida, A., Yamagata, T., 2004. Can Luzon Strait Transport play a role in conveying the impact of ENSO to the South China Sea? Journal of Climate 17, 3644–3657.

Rio, M.-H., Schaeer, P., Moreaux, G., Lemoine, J.-M., Bronner, E., 2009. A new Mean Dynamic Topography computed over the global ocean from GRACE data, altimetry and in-situ measurements. In: OceanObs'09, Venice, Italy.

Roemmich, D., Gilson, J., 2009. The 2004–2008 mean and annual cycle of temperature, salinity, and steric height in the global ocean from the Argo Program. Progress in Oceanography 82, 81–100.

Shen, M.-L., 2009. Interaction of Ocean Waves and Offshore Structures: A numerical comprehension. Verlag Dr. Müller.

Shen, M.-L., Huang, C.-J., 2008. Simulation of random waves and associated laminar bottom shear stresses. China Ocean Engineering 22, 477–490.

Shen, M.-L., Tseng, Y.-H., Jan, S., 2011. The formation and dynamics of the cold-dome off northeast of Taiwan. Journal of Marine Systems 86, 10–27.

Solomon, A., 2010. Interannual ENSO variability forced through coupled atmosphere–ocean feedback loops. Geophysical Research Letters 37, L02706.

Swanson, D.C., 2000. Signal Processing for Intelligent Sensor Systems. Marcel Dekker.

Tang, T.-Y., Hsueh, Y., Yang, Y.J., Ma, J.C., 1999. Continental slope flow northeast of Taiwan. Journal of Physical Oceanography 29, 1353–1362.

Tang, T.-Y., Tai, J.-H., Yang, Y.-J., 2000. The flow pattern north of Taiwan and the migration of the Kuroshio. Continental Shelf Research 20, 349–371.

Tierney, C., Wahr, J., Bryan, F., Zlotnicki, V., 2000. Short-period oceanic circulation: implications for satellite altimetry. Geophysical Research Letters 27, 1255–1258.

Tseng, Y.-H., Dietrich, D.E., Ferziger, J.H., 2005. Regional circulation of the Monterey Bay region: hydrostatic versus nonhydrostatic modeling. Journal of Geophysical Research 110, C09015.

Tseng, Y.-H., Jan, S., Dietrich, D.E., Lin, I.-I., Chang, Y.-T., Tang, T.-Y., 2010. Modeled oceanic response and sea surface cooling to Typhoon Kai-Tak. Terrestrial Atmospheric and Oceanic Sciences 21, 85–98. http://dx.doi.org/10.3319/TAO.2009.06.08.02.

Tseng, Y.-H., Shen, M.-L., Jan, S., Dietrich, D.E., Chiang, C.-P., 2012. Validation of the Kuroshio Current system in the dual-domain Pacific ocean model framework. Progress in Oceanography 105, 102–123.

Tzeng, W.-N., Tseng, Y.-H., Han, Y.-S., Hsu, C.-C., Chang, C.-W., Di Lorenzo, E., Hsieh, C.-H., 2012. Evaluation of multi-scale climate effects on annual recruitment levels of the Japanese Eel, Anguilla Japonica, to Taiwan. PLoS ONE 7, e30805. http://dx.doi.org/10.1371/journal.pone.0030805.

Vinogradova, N.T., Ponte, R.M., Stammer, D., 2007. Relation between sea level and bottom pressure and the vertical dependence of oceanic variability. Geophysical Research Letters 34, L03608.

Wang, Q.-Y., Hu, D.-X., 2006. Bifurcation of the North Equatorial Current derived from altimetry in the Pacific Ocean. Journal of Hydrodynamics 18, 620–626.

Yang, Y., Liu, C.-T., Hu, J.-H., Koga, M., 1999. Taiwan Current (Kuroshio) and impinging eddies. Journal of Oceanography 55, 609–617.

Young, C.-C., Tseng, Y.-H., Shen, M.-L., Liang, Y.-C., Chen, M.-H., Chien, C.-H., 2012. Software development of the Talwan Multi-scale Community Ocean Model (TIMCOM). Environmental Modelling & Software 38, 214–219.

Yu, Z., Shen, S., McCreary, J.P., Yaremchuk, M., Furue, R., 2007. South China Sea throughflow as evidenced by satellite images and numerical experiments. Geophysical Research Letters 34, L01601.

Zhang, D., Lee, T.N., Johns, W.E., Liu, C.-T., Zantopp, R., 2001. The Kuroshio east of Taiwan: modes of variability and relationship to interior ocean mesoscale eddies. Journal of Physical Oceanography 31, 1054–1074.

Zhang, D., Johns, W.E., Lee, T.N., 2002. The seasonal cycle of meridional heat transport at 24°N in the North Pacific and in the global ocean. Journal of Geophysical Research 107 (C7). http://dx.doi.org/10.1029/2001JC001011.